Exploring the Role of Ligand Connectivity in MOFs Mechanical Stability: The Case of MIL-100(Cr)

Anna Celeste, Pierre Fertey, Jean-Paul Itié, Gabriela Blanita, Claudia Zlotea, Francesco Capitani

Exploring the role of ligand connectivity in MOFs mechanical stability: the case of MIL-100(Cr)

Anna Celeste[1,2†], Pierre Fertey[2], Jean-Paul Itié[2], Gabriela Blanita[3], Claudia Zlotea[1], Francesco Capitani[2*]

[1] Institut de Chimie et des Matériaux Paris-Est, CNRS UMR 7182, UPEC, 2-8, rue Henri Dunant, 94320 Thiais, France

[2] Synchrotron SOLEIL, L'Orme des Merisiers, Départementale 128, 91192 Saint-Aubin,, France

[3] National Institute for Research and Development of Isotopic and Molecular Technologies, 67-103 Donat Str., RO-400293 Cluj-Napoca, Romania

KEYWORDS: Metal-organic frameworks, high pressure, linker, mechanical stability.

ABSTRACT: The key parameters governing the mechanical stability of highly porous materials such as metal-organic frameworks (MOFs) are yet to be clearly understood. This study focuses on the role of the linker connectivity, by investigating the mechanical stability of MIL-100(Cr), a mesoporous MOF with a hierarchical structure and a tritopic linker, and comparing it to MIL-101(Cr) having instead a ditopic linker. Using synchrotron X-ray diffraction and infrared spectroscopy we investigate the high-pressure behavior of MIL-100(Cr) with both solid and fluid pressure transmitting media (PTM). In the case of a solid medium, MIL-100(Cr) undergoes amorphization at about 0.6 GPa, while silicone oil as a PTM delays amorphization until 12 GPa due to the fluid penetration into the pores. Both these values are considerably higher than those of MIL-101(Cr). MIL-100(Cr) also exhibits a bulk modulus almost ten times larger than MIL-101(Cr). This set of results coherently proves a superior stability of MIL-100(Cr) under compression. We ascribe this to the higher connectivity of the organic linker in MIL-100(Cr), which enhances its interconnection between metal nodes. These findings shed light on the importance of linker connectivity in the mechanical stability of MOFs,a relevant contributoin to the quest for designing more robust MOFs.

INTRODUCTION

Understanding and improving the mechanical stability of a material is often a critical aspect. This is especially true in the context of metal-organic frameworks (MOFs), a class of crystalline materials wherein metal ions or clusters are coordinated with organic ligands in a precisely engineered manner.[1] MOFs have garnered significant attention due to their guest-accessible porosity, which renders them well-suited for a wide spectrum of purposes, including hydrogen storage[2], catalysis, nanoparticles incorporation[3], and drug delivery[4], among others. For such applications, MOFs must be stable, namely the structure must resist to degradation once exposed to operating conditions.[5] In particular, mechanical stability is of paramount importance for postsynthetic processing through mechanical compression.[6] Indeed, most of the MOFs are synthesized as fine powders and then densified in the form of monoliths and/or pellets for targeted operations. Determining whether the structure or textural properties are preserved during the compression or not is thus crucial.[7] In the last years, great attention has been paid to synthesizing frameworks chemically and thermally stable and different experimental approaches have been used to assess these stabilities.[5,6,8] On the contrary, mechanical stability has been determined only for a few MOFs, mainly microporous, and the systematic investigation of many new synthesized frameworks is currently lacking.[6]

The mechanical properties of a given framework can be assessed by evaluating its response to compression, shear stress or tension. In particular, applying an external pressure while tracking the volume reduction is an effective way to obtain the bulk modulus (K) of a crystalline material, which evaluates the isotropic volumetric elasticity on compression.[9] Moreover, it is possible to establish the maximum load that the system can hold before changing its phase or structure. For MOFs, this upper limit of the mechanical stability is typically marked by an amorphization process, characterized by partial or total pore collapse.[10] Given the large number of attainable frameworks, elucidating interdependencies among structural parameters—such as topology, pore volumes, and ligand connectivity— and mechanical properties, could foster the synthesis of more robust MOFs.[11,12]

As the number of reported structural parameters for compressed MOFs grows, few studies permit cross-comparisons.[11] This is due to different experimental methods or the lack of experimental details. As an example, reported values of the UiO-66(Zr) bulk modulus span between 15 and 37.9 GPa.[13–18] Such different values are probably the result of different defect concentrations present in the framework, burdensome quantity to determine experimentally.[11,15,19] Moreover, it is well known how guest molecules can penetrate into the pores and significantly impact the high-pressure behavior of MOFs and thus the bulk moduli reported in the literature.[11,20–24] A recent study by Redfern and coworkers

explores the relationship between the structural parameters of two isoreticular MOF series, the UiO and the NU-900 series. They observe that for both topologies, the bulk modulus is inversely correlated with void fraction[13], which is in agreement with a computational study showing that the bulk modulus is inversely proportional to the pore diameter for 3000 frameworks.[25] However, Redfern et al. also showed that the linker length and the nearest node distance play an important role in the framework response to compression, highlighting how even minor differences in the structure can strongly affect the bulk modulus.[13] One of the key parameters in MOFs structure that defines their topology is the linker connectivity, also known as topicity, which identifies how many metal nodes a single linker molecule can connect to within the MOF network.[16,26] Identifying MOFs with the same topology and different linker topicity and comparing their behavior at high pressure, could help in assessing the role played by this parameter in the framework mechanical stability.[11]

To contribute a piece to this puzzle, we report the study of the high-pressure behavior of the mesoporous MOF MIL-100(Cr) which presents a hierarchical structure made up of trimeric chromium oxide secondary building units (SBUs) linked by 1,3,5-benzenetricarboxylic acid (BTC).[27] MIL-100(Cr) exhibits the **mtn** topology and cubic symmetry (space group $Fd\bar{3}m$), akin to MIL-101(Cr) previously investigated at high-pressure.[20] However, it features a tritopic linker, in contrast to the ditopic 1,4-benzenedicarboxylate acid (BDC) ligand found in MIL-101(Cr).[28] In MIL-100(Cr) the chromium clusters are assembled in supertetrahedra (ST), as shown in Figure 1, and then further linked in a vertex-sharing manner forming two quasi-spherical cages. The small cage made of 20 ST has pentagonal windows of 5 and 9 Å diameter, and the large cage consisting of 28 ST shows a diameter of 29 Å accessible through hexagonal (14.7 x 16 $Å^2$) and pentagonal windows.[27]

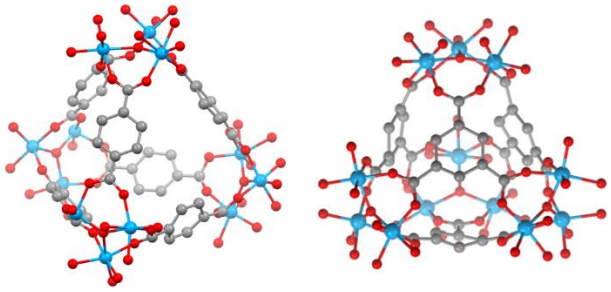

FIGURE 1 Supertetrahedra of MIL-101(Cr) (left) and MIL-100(Cr) (right). Cr, C and O atoms are depicted in blue, gray and red respectively.

Here, we investigate MIL-100(Cr) by means of synchrotron X-ray diffraction (XRD) and infrared (IR) spectroscopy at high-pressure, which is generated by diamond anvil cells (DACs) using solid and fluid pressure transmitting media (PTM). A thorough experimental procedure allowed us to compare the results obtained here with the mechanical properties of MIL-101(Cr). We demonstrate that MIL-100(Cr) presents a bulk modulus almost ten times higher than that of MIL-101(Cr), making MIL-100(Cr) the more mechanically stable mesoporous MOF reported so far.

EXPERIMENTAL SECTION

MIL-100(Cr) (chemical formula $Cr_3O(H_2O)_2F[C_6H_3(CO_2)_3]_2(H_2O)_n$ with n~28) is synthesized by a modified hydrothermal synthesis developed by Llewellyn et al.[29] Trimesic acid (8.4 g, 40 mmol), HF 49% (1.44 ml, 0.8 g, 40 mmol HF) and H_2O (192 ml) are added to CrO_3 (4 g, 4 mmol). The obtained mixture is stirred for a few minutes at room temperature and then introduced in a Teflon-lined stainless-steel autoclave for 96 hours at 493 K. The resulting green solid is separated by filtration, washed with water, and dried at 393 K in an oven. The as-synthesized MIL-100(Cr) is purified by Soxhlet extraction with ethanol. Nitrogen porosimetry was performed at 77 K to estimate its textural properties (see Figure S1 in Supporting Information). The determined BET surface area and the specific pore volume are 1679±10 m^2g^{-1} and 0.92±0.01 $cm^3\ g^{-1}$ respectively. Transmission electron microscopy images shows that the crystallite size of the MIL-100(Cr) is in between 100 and 200 nm (see Figure S2). The thermal stability of MIL-100(Cr) was determined by thermogravimetric analysis (TGA), shown in Figure S3.

Since activated samples can easily adsorb water molecules, samples have been degassed before any experiment at 493 K for 18 hours under vacuum (below 10^{-5} mbar) and successively handled avoiding air exposure, *i.e.* in a glovebox under an N_2 gas atmosphere with O_2 and H_2O levels below 1 ppm, before the high-pressure experiments.

The crystalline structure of activated MIL-100(Cr) was verified by both laboratory and synchrotron X-ray diffraction at ambient conditions. Laboratory measurements have been performed on samples exposed to air, using a Bruker-D8 Advance diffractometer in the Bragg-Brentano geometry and using as source a copper anticathode ($\lambda K_{\alpha 1}$ = 1.5406 Å) fed at 40 kV and 40 mA (Figure S4). An additional high-resolution diffractogram of a degassed sample has been collected at the CRISTAL beamline of the SOLEIL synchrotron (Figure S5). Diffraction images were collected using Rayonix SX165 detector a monochromatic beam with a wavelength of 0.7293 Å.

Synchrotron high-pressure measurements were carried out at SOLEIL synchrotron. Membrane DACs equipped with IIas diamonds were used. The sample chambers consisted of a 150−200 µm hole drilled in pre-indented stainless-steel gaskets 50 µm thick. For each experimental run, the activated samples were loaded into the DAC in a glovebox equipped with a microscope and the DAC was sealed at the lowest pressure achievable, usually around 0.01-0.1 GPa, before removing it from the glovebox. Fluid and solid PTM were used in separate experiments: PDMS silicone oil (polydimethylsiloxane / PDMS, viscosity 30 000 cSt at 300 K, CAS 63148-62-9) and alkali salts, namely, NaCl for XRD and CsI for IR, chosen for its transparency in the far infrared region.[30] Before being loaded, solid PTM were finely milled and stored in an oven at 393 K. In the case of XRD experiments, the sample was loaded together with the chosen PTM and few grains of NaCl, used to determine the pressure from its equation of state. The XRD experimental run with silicone oil was performed on the PSICHE beamline using a wavelength of 0.485930 Å, a spot size of 35x35 $µm^2$and a DECTRIS CdTe 4 M detector. XRD measurements with NaCl as PTM were collected on the CRISTAL beamline with a

0.5802 Å X-ray beam, a spot of around 40 μm², and a Rayonix SX165 detector. Raw diffraction images were corrected by masking, if any, diamond reflections, and artifacts and converted to 1D patterns by using the Dioptas software.[31] Unit cell parameters were then refined using the Le Bail method. The equation of state fitting procedure has been performed using the EoS fit software.[32]

IR spectroscopy measurements were performed at the SMIS beamline with a home-built horizontal microscope equipped with custom Schwarzschild objectives and coupled to a Thermo Fisher iS50 Fourier-transform spectrometer. Mid-IR (MIR) spectra (700 – 4000 cm^{-1}) were collected with a liquid N_2-cooled MCT detector while a liquid He-cooled Si bolometer was used to collect far-IR (FIR) spectra in the 200 – 700 cm^{-1} spectral range. KBr and solid substrate beam splitters were used for these two spectral ranges. Peak frequencies and width were obtained via least-square fitting using Lorentzian functions. For all experimental runs, pressure was increased at a rate of about 0.02 GPa per minute and it was obtained by the ruby fluorescence technique.

RESULTS AND DISCUSSION

Selected diffractograms of MIL-100(Cr) collected with increasing pressure are reported in Figure 2 using NaCl and silicone oil as PTM. In the NaCl case (panel (a)), the intensity of the Bragg peaks gradually decreases on compression up to about 0.6 GPa. This indicates a complete transition to an amorphous phase which is not reversible after the pressure release. On the contrary, when silicone oil is used as PTM (panel (b)), the main XRD peaks are still detectable, although very broad, up to around 18 GPa pointing out that some crystalline long-range order is still present at this pressure.

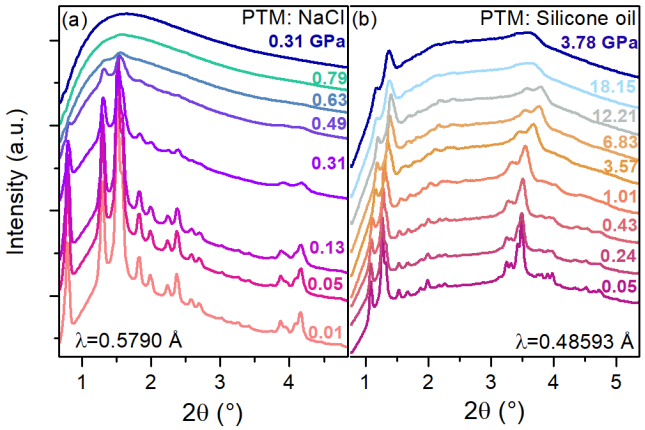

FIGURE 2 Selected powder XRD patterns of MIL-100(Cr) under pressure with (a) NaCl (λ=0.5790 Å) and (b) silicone oil (λ=0.48593 Å). Patterns are vertically stacked for the sake of clarity. Patterns collected after the pressure release are shown in blue.

The pattern collected at the minimum pressure obtained after the pressure release, *i.e.* around 3.8 GPa, resembles those measured at the highest pressure. This means that the original crystalline order is not re-established. However, a complete transition to an amorphous phase is not observed with the fluid PTM in the pressure range explored. The pressure dependence of the lattice parameter of MIL-100(Cr) is reported in Figure 3(a) in the low-pressure range. In the case of solid PTM, *a* decreases on compression quite regularly up to around 0.4 GPa. Above this pressure value the slope changes slightly concomitantly with the abrupt loss of the Bragg peaks intensity in the XRD patterns (see Figure 2(a)), suggesting that this effect is probably linked to the onset of the amorphization, then completed around 0.6 GPa.

We performed a fit to the unit cell volume data with a second and third-order Birch-Murnaghan equation of state (EoS)[33] up to 0.4 GPa, as shown in Figure 3(b). In the case of a second-order EoS (dotted red line), the bulk modulus results to be K_0 = 9.0±0.4 GPa. Although the fit converged, the curve obtained does not perfectly match the experimental points. For this reason, we also tested a third-order equation (dashed red line) which gave a bulk modulus K_0 = 12.0±0.4 GPa and its first derivative K_p = -8.6±1.4 GPa. A negative value for K_p indicates that the framework becomes more compressible on increasing pressure, an unusual effect for solid systems. However, a similar response has been previously reported for ZIF-8.[34] The authors proposed that this could originates from the bending of the organic linker and may be a widespread phenomenon for hybrid porous materials.[34]

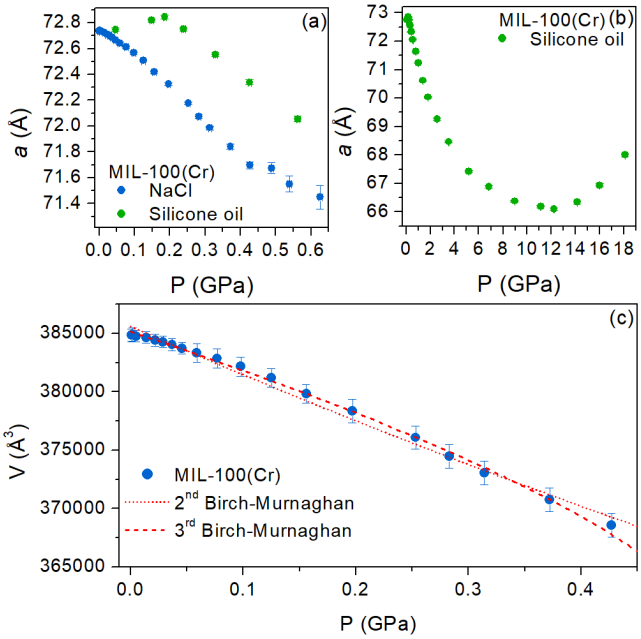

FIGURE 3 Pressure dependence of MIL-100(Cr) lattice parameter a up to (a) 0.65 GPa and to (b) 19 GPa. NaCl (pale blue symbols) and silicone oil (light green) are the PTM employed. If not displayed, error bars are within the symbol size. (c) Unit cell volume of MIL-100(Cr) in the 0-0.5 GPa pressure range. Dotted and dashed red lines represent the second and third-order Birch-Murnaghan equation-of-state fit of the experimental points, respectively.

With silicone oil as the PTM, a quite different pressure dependence of the lattice parameter is observed. As shown in Figure 3(a), it slightly increases up to 0.2 GPa, and then starts to decrease with pressure. The unusual volume expansion of the unit cell could be explained by a pressure-promoted hyperfilling of the MIL-100(Cr) pores by the PDMS, as already observed for MIL-101(Cr) at a lower extent.[20] Indeed, the bulky polymeric chains of PDMS would require high pressures to be inserted into the pores causing

the volume expansion up to about 0.2 GPa. After this pressure value, MIL-100(Cr) and the silicone oil are compressed together up to 12 GPa and the whole pressure behavior originates from the composite material. Above 12 GPa, the lattice parameter starts to increase (see Figure 3(b)), which has also been seen in the MIL-101(Cr) case, and signals the formation of an amorphous phase denser than the crystalline phase, thus freeing some spaces inside the DAC gasket hole to allow for the observed expansion of the crystalline sample portion.[20]

To test the hypothesis of the fluid PTM presence inside the pores, we measured the IR spectra of MIL-100(Cr) under pressure in the spectral range spanning the FIR and the MIR, *i.e.* from 100 to 5000 cm^{-1} with the two PTM used. Details of the peak assignments, some of them here reported for the first time, are discussed in the SI (figures S6 and S7).

Here we focus on the FIR (200 – 700 cm^{-1}) range, where collective and CrO vibrational modes appear, and on the high-frequency region of the MIR (3500 – 3750 cm^{-1}) characterized by OH stretching modes. These two spectral regions at high-pressure are reported in Figure 4 panels (a)-(b), where CsI is the PTM, and in panels (c)-(d), with silicone oil as PTM. In the first case, the peaks broaden and their intensity decreases under pressure. In particular, the OH ν_{26} – ν_{28} modes are completely suppressed and not detectable anymore above 0.7 GPa, while the intensity reduction of collective and CrO ν_1 – ν_4 peaks stops above this pressure threshold. The spectrum collected after releasing pressure, shown in blue in Figure 4, indicates a preservation of the pressure-induced modifications, which agrees with the irreversible transition to the amorphous phase observed at around 0.6 GPa in the XRD experiments.

Focusing now on the silicone oil case, spectra shown in Figure 4(c)-(d) present a quite different evolution under pressure: the CrO ν_4 mode blueshifts without a noticeable intensity variation until 6 GPa, followed by a broadening. A broad OH mode redshifts until it merges with the broad band detected between 2700 and 3500 cm^{-1} attributed to interacting residual water molecules inside the pores.[35] Indeed, it is worth noting that even after degassing the sample, which removes the majority of water molecules, a small percentage persists within the pores. After the pressure release, the observed effects at high-pressure are almost fully reversible. These spectroscopic results are thus consistent with the those found by XRD, pointing out the structural endurance of the framework up to 18 GPa (see Figure 2(b)) with silicone oil.

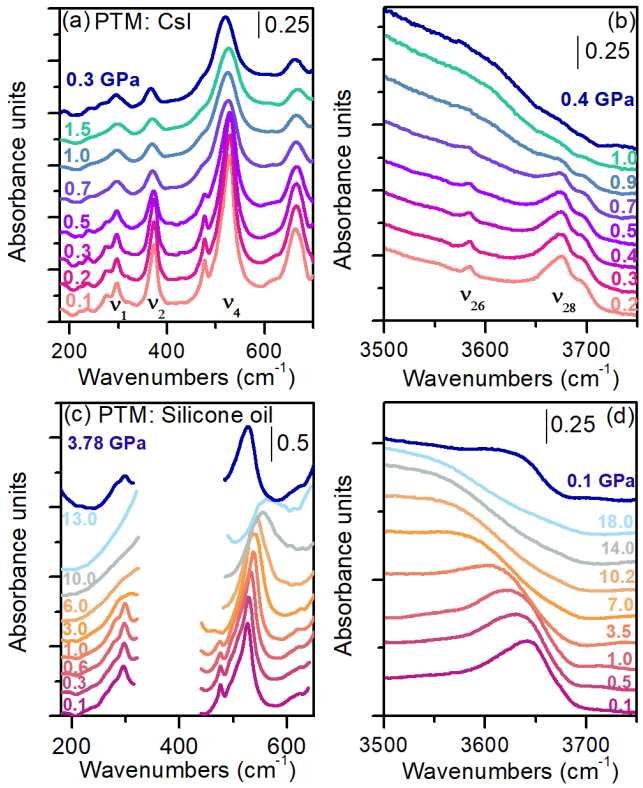

FIGURE 4 FIR and OH stretching regions of MIL-100(Cr) spectra measured under pressure with CsI(a)-(b) and silicone oil (c)-(d) used as PTM. In panel (c), the absorption of around 400 cm^{-1} of silicone oil is masked (see figure S8 for a spectrum of silicone oil). Spectra collected after the pressure release, at the lowest possible pressure, are shown in blue. Spectra are vertically stacked for clarity with increasing pressure values.

To quantify the reported spectral changes, we extracted by a fitting procedure the peak frequency and the full width at half maximum (FWHM) of the CrO mode ν_4 and the OH ν_{26} peak, which is assigned to the structural hydroxyl group linked to the chromium atoms of the metallic cluster.[35] The pressure dependence of these parameters is shown in Figure 5 up to 1.1 GPa for both PTM, where the peak frequency and the FWHM of the ν_{26} mode have been normalized to the value obtained at the lowest pressure measured to ease the comparison (absolute values are shown in figures S10 and S11).

In the silicone oil case (green symbols), ν_4 mode hardens and ν_{26} mode softens under pressure while the FWHMs remain quite constant without showing any relevant anomaly, consistently with the absence of phase transitions. Instead, when using a solid PTM (blue symbols), the CrO mode ν_4 hardens up to around 0.4 GPa, then it softens until it is finally stabilized around 522 cm^{-1} above 0.8 GPa as shown in panel (a) of Figure 5. The OH mode frequency ν_{26} is quite stable before becoming undetectable at 0.8 GPa. Indeed, both FWHMs of ν_4 and ν_{26} modes show a clear and sudden slope change at about 0.4 GPa with a strong increase persisting up to 0.8 GPa, where the width of the CrO mode stabilizes, similarly to its frequency trend.

The effects observed around 0.4 GPa with the solid medium can be related to the occurrence of the crystal-to-

amorphous transition, where the pore collapse and lattice distortions increase the interaction among adjacent atoms, thus abruptly increasing the peak widths[36] and weakening the CrO bonds. The changes around 0.8 GPa thus signal the end of the crystal-amorphous conversion. The absence of hardening for the OH modes, thus contrary to the usual response of vibrational modes under pressure, could be explained by the formation and strengthening of hydrogen bonds between the hydroxyl groups and the neighboring C-H groups of the organic linker[37] which are made possible by the dramatic distortions that the framework experience during the amorphization process. Filling the pore voids with PDMS removes all the aforementioned spectroscopic signatures from the pressure dependence of the MIL-100(Cr) peak parameters. Indeed, now they evolve smoothly under pressure, clearly indicating the lack of abrupt and dramatic structural changes. It is worth noting the strong softening of the OH frequency, nicely explained by the distance between the hydroxyl groups and the guest polymers getting reduced by pressure, which increases the hydrogen-PDMS interaction thus weakening the OH bond. Therefore, the OH frequency vs pressure relation, is a clear marker of the host-guest interaction.

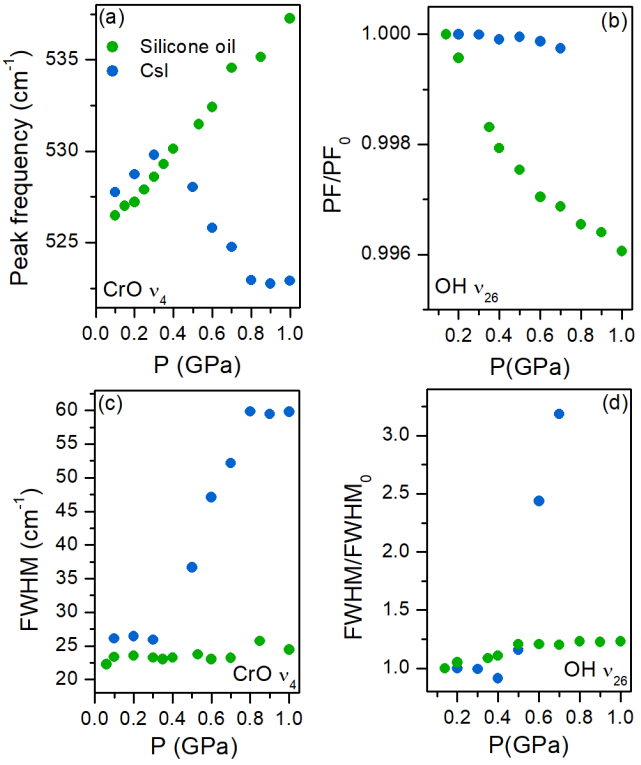

FIGURE 5 Pressure dependence of the peak frequencies (PF) and full-widths-half-maximum (FWHM) of the CrO ν_4 (a)-(c) and the OH ν_{26} (b)-(d) modes of MIL-100 up to 1.1 GPa with different PTM: CsI (pale blue symbol) and silicone oil (green). For the OH modes, the PF and FWHM values at each pressure have been normalized to those at the initial pressure, PF_0 and $FWHM_0$. Error bars are within the symbol size.

Finally, the whole set of IR data confirms that the pressure induced transition to the amorphous phase starts around 0.4 GPa and it is completed around 0.8 GPa when no guests are present in the pores, in agreement with the results obtained by XRD. The small discrepancy in the pressure values for the end of the amorphization obtained through the two techniques, probably originates from the higher sensitivity of IR spectroscopy to the local environment. The discrepancy suggests that short-range order is still present after the amorphization, between 0.6 and 0.8 GPa, when instead the long-range order is completely lost.[38]

This coherent set of results on MIL-100(Cr) at high-pressure allows for a comparison with MIL-101(Cr).[20,21] MIL-100(Cr) has a similar cubic structure and the same topology as MIL-101(Cr) consisting of microporous supertetrahedral units linked by rigid carboxylate ligands: trimesate and terephthalate, respectively.[27,28] The presence of a different linker results in different pore sizes and windows which in turn is reflected in the internal surface areas and total pore volumes: MIL-101(Cr) displays larger pores and higher total pore volume compared to MIL-100(Cr).

The comparison between the present results on MIL-100(Cr) and those on MIL-101(Cr)[20,21] shows that they behave qualitatively similarly when an external pressure is applied. When a solid medium is employed, an irreversible amorphization of the empty structure occurs for both systems. However, a closer inspection reveals quantitative differences. MIL-100(Cr) bulk modulus is considerably higher, almost 9 times in the case of the second-order equation of state fit, and the amorphization occurs at higher pressure, being completed around 0.6 GPa for MIL-100(Cr) instead of 0.1 GPa for MIL-101(Cr). This is particularly noticeable when the normalized unit cell volumes of the two frameworks are compared under pressure, as shown in Figure 6(a). An analogous comparison with silicone oil as PTM is shown in Figure 6(b). The overall behavior of the two mesoporous MOFs appears similar to an initial compression of the volume followed by the increase observed concurrently with the amorphization onset. However, this effect is shifted to higher pressure for MIL-100(Cr).

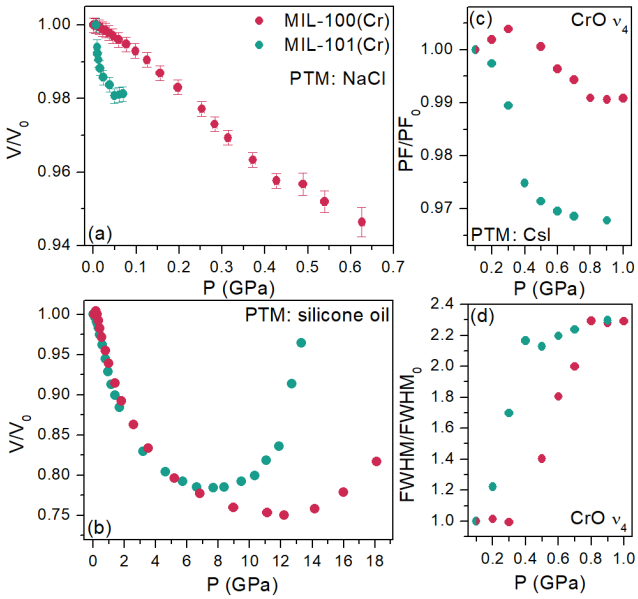

FIGURE 6 Unit cell volume as a function of the pressure for MIL-101(Cr) (green) and MIL-100(Cr) (red) when NaCl (a) and silicone oil (b) are employed as medium. Pressure dependences of CrO peak frequency (PF) (c) and width (FWHM) (d) for both samples with a solid PTM. Volume, peak frequency, and width values are normalized to the

lowest pressure values for each sample. MIL-101(Cr) data are from our previous works.[20,21]

At a local scale, both frameworks feature the same chromium oxide SBUs and this is reflected in a qualitatively similar behavior of the peak parameters of the CrO mode (ν_4) under pressure with a solid PTM. As shown in Figure 6(c)-(d), from low to high-pressure, the frequency trend is characterized by a hardening-softening-constant sequence whereas a constant-broadening-constant sequence is observed for the width. It is interesting to notice that the initial frequency hardening, which is usually the expected response of a vibrational mode to compression, is not observed for MIL-101(Cr) because of the amorphization process taking place already at about 0.1 GPa. This qualitatively similar behavior but shifted in pressure when changing the linker, indicates that the mechanical instability, ultimately leading to the amorphization, does not probably stem from the metallic cluster, i.e., the trimeric chromium oxide SBU, but from the linker.

Previous experimental and theoretical studies prove that also other structural parameters, such as the length and shape of the linker, the metallic node connectivity or different metallic ions, affect the framework stability.[9,13,37,39,40] The influence of the ligand topicity on the mechanical stability has never been explored before, to the best of our knowledge. Our results indicate that the polytopic nature of the BTC linker and the higher interconnection between the metal SBUs in MIL-100(Cr) are key factors in achieving higher mechanical stability in porous frameworks. As a comparison, augmenting node connectivity in NU-901 by introducing an extra linker, resulted in a less than twofold increase of the bulk modulus.[40] Conversely, in the case of UiO-66 with different metals, the variation in bulk modulus was smaller than a factor of two.[37] This underscores the significantly greater impact of linker topicity on the mechanical stability, as reported here for MIL-100 and MIL-101.

To further enlarge our discussion, we report in Table 1 bulk modulus and other relevant structural parameters for noteworthy MOFs previously studied at high pressure.

TABLE 1 Void fraction, linker length, bulk modulus K_0 and amorphization pressures (AP) for various MOFs, including MIL-100(Cr) and MIL-101(Cr), ordered by decreasing void fractions. References are indicated for each value.

MOFs	Void fraction	Linker length (Å)	K_0 (GPa)	AP (GPa)
MIL-101(Cr)	0.83[28]	6.02[13]	1.1±0.9[21]	0.1[21]
MIL-100(Cr)	0.76[27]	5.05[27]	9.0±0.4	0.6
PCN-57(Zr)[13]	0.73	14.35	4.6±0.1	> 0.3
NU-901(Zr)[13]	0.70	17.08	7.2±0.3	> 0.3
HKUST-1	0.68[41]	5.05[41]	29.5±0.5[24]	> 2[24]
MIL-125(Ti)	0.68[42]	6.02[13]	10±2[14]	> 2[14]
UiO-67(Zr)[13]	0.64	10.09	21.1±0.6	> 0.25
DUT-52(Zr)[13]	0.57	7.99	17±2	NA
UiO-66(Zr)	0.52[13]	6.02[13]	37.9±0.6[13]	1.8[18]

To ensure a meaningful comparison, our analysis focused on MOFs having BDC and BTC linkers, such as UiO-66, MIL-125 and HKUST-1, in addition to MOFs showing a correlation between void fraction (or linker length) and bulk modulus. [13] Indeed, Redfern et al. hypothesized that the primary source of lattice rigidity was due to the steric repulsion of the framework components: the presence of larger void, i.e. larger void fraction, thus leads to a lower mechanical stability.[13] Our data on MIL-100(Cr) and MIL-101(Cr) align with this qualitative correlation showing that the bulk modulus decreases as the void fraction increases (see Table 1 and Figure S12). However, it is worth noticing a slight deviation in the case of MIL-100(Cr) and HKUST-1, which display a higher bulk modulus although having a void fraction comparable to that of MOFs with a BDC linker. i.e. MIL-101(Cr) and MIL-125(Ti), respectively. This stresses, once more, the importance of the linker topicity. although totally decoupling this parameter and the textural properties, in particular the void fraction, is not possible. Nevertheless, comparing the high-pressure behavior of the two MOFs when their pores are filled with a fluid PTM could be a first step in disentangling the porosity and the linker connectivity. As shown in Figure 6(b), the MIL-100(Cr) volume starts to increase around 12 GPa, 5 GPa higher than in MIL-101(Cr), thus highlighting a higher mechanical stability of the MIL-100(Cr) backbone structure even when the pores are filled. We can thus conclude that the higher mechanical stability of MIL-100(Cr) compared to MIL-101(Cr) originates from the higher linker connectivity.

CONCLUSIONS

In this work, we investigated the mechanical stability of a mesoporous MOFs, *i.e.* MIL-100(Cr), using solid and fluid PTM revealing the pressure-induced modification of its structural and vibrational properties. Exploiting two complementary techniques, X-ray diffraction and infrared spectroscopy, and carrying out a thorough sample preparation provided a clear and coherent picture about the intrinsic mechanical stability of the system, the effect of eventual guests inside the pores, and the role played by the ligand connectivity. In the case of solid PTM, MIL-100(Cr) undergoes amorphization at 0.6 GPa, higher than the pressure value of 0.1 GPa observed for MIL-101(Cr), showing that MIL-100(Cr) presents a superior mechanical stability than MIL-101(Cr). Accordingly, MIL-100(Cr) exhibits a considerably higher bulk modulus, about ten times greater than the one obtained for MIL-101(Cr). These two MOFs have the same topology but an organic linker with different connectivities, *i.e.* two for MIL-101(Cr) and three for MIL-100(Cr). Although the linker connectivity and the porosity are inevitably correlated, our results point out that a polytopic linker in the framework provides higher mechanical stability. Therefore, we hope that this study stimulates further high-pressure investigation focusing on MOFs with different linker connectivities but similar pore volumes to disentangle these two parameters and find the structural key to achieving mesoporous MOFs with higher mechanical stability to compression.

ASSOCIATED CONTENT

Supporting Information.

N_2 adsorption and desorption measurements, TEM images, thermogravimetric analysis, XRD measurements at ambient conditions, infrared characterization at ambient conditions and peak assignments, infrared spectrum of silicone oil, pressure dependence of vibrational modes.

AUTHOR INFORMATION

Corresponding Author

Francesco Capitani – Synchrotron SOLEIL, 91192 Cedex Gif sur Yvette, France; orcid.org/0000-0003-1161-7455; Email: francesco.capitani@synchrotron-soleil.fr

Present Addresses

† Department of Earth and Planetary Science, Stanford University, Stanford, CA 94305, USA

Funding Sources

A.C, C.Z. and G.B. acknowledge the French National Research Agency (ANR) and the Romanian Ministry of Education and Research (UEFISCDI) for the financial support under MEMOS contract ANR-15-CE05-0012-01 and PN-II-ID-JRP-RO-FR-2015-0025, respectively.

Notes

The authors declare no competing financial interest.

ACKNOWLEDGMENT

The authors gratefully acknowledge synchrotron SOLEIL (proposals #20190878, #20201415 and #20200412) for the provision of beamtime. Alain Polian and Oana Grad are acknowledged for their help in the experimental preparation while Julie Bourgon for performing TEM characterization. The authors thank A. Last from the Institute of Microstructure Technology of the Karlsruhe Nano-Micro Facility for providing a polymer X-ray lenses transfocator to horizontally focus the X-ray beam on the CRISTAL beamline.

REFERENCES

(1) Rowsell, J. L. C.; Yaghi, O. M. Metal–Organic Frameworks: A New Class of Porous Materials. *Microporous Mesoporous Mater.* **2004**, *73* (1), 3–14. https://doi.org/10.1016/j.micromeso.2004.03.034.

(2) Chen, Z.; Kirlikovali, K. O.; Idrees, K. B.; Wasson, M. C.; Farha, O. K. Porous Materials for Hydrogen Storage. *Chem* **2022**, *8* (3), 693–716. https://doi.org/10.1016/j.chempr.2022.01.012.

(3) Falcaro, P.; Ricco, R.; Yazdi, A.; Imaz, I.; Furukawa, S.; Maspoch, D.; Ameloot, R.; Evans, J. D.; Doonan, C. J. Application of Metal and Metal Oxide nanoparticles@MOFs. *Coord. Chem. Rev.* **2016**, *307*, 237–254. https://doi.org/10.1016/j.ccr.2015.08.002.

(4) Lawson, H. D.; Walton, S. P.; Chan, C. Metal–Organic Frameworks for Drug Delivery: A Design Perspective. *ACS Appl. Mater. Interfaces* **2021**, *13* (6), 7004–7020. https://doi.org/10.1021/acsami.1c01089.

(5) Yuan, S.; Feng, L.; Wang, K.; Pang, J.; Bosch, M.; Lollar, C.; Sun, Y.; Qin, J.; Yang, X.; Zhang, P.; Wang, Q.; Zou, L.; Zhang, Y.; Zhang, L.; Fang, Y.; Li, J.; Zhou, H.-C. Stable Metal–Organic Frameworks: Design, Synthesis, and Applications. *Adv. Mater.* **2018**, *30* (37), 1704303. https://doi.org/10.1002/adma.201704303.

(6) Ding, M.; Cai, X.; Jiang, H.-L. Improving MOF Stability: Approaches and Applications. *Chem. Sci.* **2019**, *10* (44), 10209–10230. https://doi.org/10.1039/C9SC03916C.

(7) Yeskendir, B.; Dacquin, J.-P.; Lorgouilloux, Y.; Courtois, C.; Royer, S.; Dhainaut, J. From Metal–Organic Framework Powders to Shaped Solids: Recent Developments and Challenges. *Mater. Adv.* **2021**, *2* (22), 7139–7186. https://doi.org/10.1039/D1MA00630D.

(8) Howarth, A. J.; Liu, Y.; Li, P.; Li, Z.; Wang, T. C.; Hupp, J. T.; Farha, O. K. Chemical, Thermal and Mechanical Stabilities of Metal–Organic Frameworks. *Nat. Rev. Mater.* **2016**, *1* (3), 1–15. https://doi.org/10.1038/natrevmats.2015.18.

(9) Burtch, N. C.; Heinen, J.; Bennett, T. D.; Dubbeldam, D.; Allendorf, M. D. Mechanical Properties in Metal–Organic Frameworks: Emerging Opportunities and Challenges for Device Functionality and Technological Applications. *Adv. Mater.* **2018**, *30* (37), 1704124. https://doi.org/10.1002/adma.201704124.

(10) Coudert, F.-X. Responsive Metal–Organic Frameworks and Framework Materials: Under Pressure, Taking the Heat, in the Spotlight, with Friends. *Chem. Mater.* **2015**, *27* (6), 1905–1916. https://doi.org/10.1021/acs.chemmater.5b00046.

(11) Vervoorts, P.; Stebani, J.; Méndez, A. S. J.; Kieslich, G. Structural Chemistry of Metal–Organic Frameworks under Hydrostatic Pressures. *ACS Mater. Lett.* **2021**, *3* (12), 1635–1651. https://doi.org/10.1021/acsmaterialslett.1c00250.

(12) Nandy, A.; Yue, S.; Oh, C.; Duan, C.; Terrones, G. G.; Chung, Y. G.; Kulik, H. J. A Database of Ultrastable MOFs Reassembled from Stable Fragments with Machine Learning Models. *Matter* **2023**, *6* (5), 1585–1603. https://doi.org/10.1016/j.matt.2023.03.009.

(13) Redfern, L. R.; Robison, L.; Wasson, M. C.; Goswami, S.; Lyu, J.; Islamoglu, T.; Chapman, K. W.; Farha, O. K. Porosity Dependence of Compression and Lattice Rigidity in Metal–Organic Framework Series. *J. Am. Chem. Soc.* **2019**, *141* (10), 4365–4371. https://doi.org/10.1021/jacs.8b13009.

(14) Yot, P. G.; Yang, K.; Ragon, F.; Dmitriev, V.; Devic, T.; Horcajada, P.; Serre, C.; Maurin, G. Exploration of the Mechanical Behavior of Metal Organic Frameworks UiO-66(Zr) and MIL-125(Ti) and Their NH2 Functionalized Versions. *Dalton Trans.* **2016**, *45* (10), 4283–4288. https://doi.org/10.1039/C5DT03621F.

(15) Dissegna, S.; Vervoorts, P.; Hobday, C. L.; Düren, T.; Daisenberger, D.; Smith, A. J.; Fischer, R. A.; Kieslich, G. Tuning the Mechanical Response of Metal–Organic Frameworks by Defect Engineering. *J. Am. Chem. Soc.* **2018**, *140* (37), 11581–11584. https://doi.org/10.1021/jacs.8b07098.

(16) Robertson, G. P.; Mosca, S.; Castillo-Blas, C.; Son, F. A.; Farha, O. K.; Keen, D. A.; Anzellini, S.; Bennett, T. D. Survival of Zirconium-Based Metal–Organic Framework Crystallinity at Extreme Pressures. *Inorg. Chem.* **2023**, *62* (26), 10092–10099. https://doi.org/10.1021/acs.inorgchem.2c04428.

(17) Redfern, L. R.; Ducamp, M.; Wasson, M. C.; Robison, L.; Son, F. A.; Coudert, F.-X.; Farha, O. K. Isolating the Role of the Node-Linker Bond in the Compression of UiO-66 Metal–Organic Frameworks. *Chem. Mater.* **2020**, *32* (13), 5864–5871. https://doi.org/10.1021/acs.chemmater.0c01922.

(18) Rogge, S. M. J.; Yot, P. G.; Jacobsen, J.; Muniz-Miranda, F.; Vandenbrande, S.; Gosch, J.; Ortiz, V.; Collings, I. E.; Devautour-Vinot, S.; Maurin, G.; Stock, N.; Van Speybroeck, V. Charting the Metal-Dependent High-Pressure Stability of Bimetallic UiO-66 Materials. *ACS Mater. Lett.* **2020**, *2* (4), 438–445. https://doi.org/10.1021/acsmaterialslett.0c00042.

(19) Redfern, L. R.; Farha, O. K. Mechanical Properties of Metal–Organic Frameworks. *Chem. Sci.* **2019**, *10* (46), 10666–10679. https://doi.org/10.1039/C9SC04249K.

(20) Celeste, A.; Paolone, A.; Itié, J.-P.; Borondics, F.; Joseph, B.; Grad, O.; Blanita, G.; Zlotea, C.; Capitani, F. Mesoporous Metal–Organic Framework MIL-101 at High Pressure. *J. Am.*

Chem. Soc. **2020**, *142* (35), 15012–15019. https://doi.org/10.1021/jacs.0c05882.

(21) Celeste, A.; Capitani, F.; Fertey, P.; Paolone, A.; Borondics, F.; Grad, O.; Blanita, G.; Zlotea, C. Enhanced Stability of the Metal–Organic Framework MIL-101(Cr) by Embedding Pd Nanoparticles for Densification through Compression. *ACS Appl. Nano Mater.* **2022**, *5* (3), 4196–4203. https://doi.org/10.1021/acsanm.2c00136.

(22) Collings, I. E.; Goodwin, A. L. Metal–Organic Frameworks under Pressure. *J. Appl. Phys.* **2019**, *126* (18), 181101. https://doi.org/10.1063/1.5126911.

(23) McKellar, S. C.; Moggach, S. A. Structural Studies of Metal–Organic Frameworks under High Pressure. *Acta Crystallogr. Sect. B Struct. Sci. Cryst. Eng. Mater.* **2015**, *71* (6), 587–607. https://doi.org/10.1107/S2052520615018168.

(24) Chapman, K. W.; Halder, G. J.; Chupas, P. J. Guest-Dependent High Pressure Phenomena in a Nanoporous Metal–Organic Framework Material. *J. Am. Chem. Soc.* **2008**, *130* (32), 10524–10526. https://doi.org/10.1021/ja804079z.

(25) Moghadam, P. Z.; Rogge, S. M. J.; Li, A.; Chow, C.-M.; Wieme, J.; Moharrami, N.; Aragones-Anglada, M.; Conduit, G.; Gomez-Gualdron, D. A.; Van Speybroeck, V.; Fairen-Jimenez, D. Structure-Mechanical Stability Relations of Metal-Organic Frameworks via Machine Learning. *Matter* **2019**, *1* (1), 219–234. https://doi.org/10.1016/j.matt.2019.03.002.

(26) O'Keeffe, M.; Yaghi, O. M. Deconstructing the Crystal Structures of Metal–Organic Frameworks and Related Materials into Their Underlying Nets. *Chem. Rev.* **2012**, *112* (2), 675–702. https://doi.org/10.1021/cr200205j.

(27) Férey, G.; Serre, C.; Mellot-Draznieks, C.; Millange, F.; Surblé, S.; Dutour, J.; Margiolaki, I. A Hybrid Solid with Giant Pores Prepared by a Combination of Targeted Chemistry, Simulation, and Powder Diffraction. *Angew. Chem. Int. Ed.* **2004**, *43* (46), 6296–6301. https://doi.org/10.1002/anie.200460592.

(28) Férey, G.; Mellot-Draznieks, C.; Serre, C.; Millange, F.; Dutour, J.; Surblé, S.; Margiolaki, I. A Chromium Terephthalate-Based Solid with Unusually Large Pore Volumes and Surface Area. *Science* **2005**, *309* (5743), 2040–2042. https://doi.org/10.1126/science.1116275.

(29) Llewellyn, P. L.; Bourrelly, S.; Serre, C.; Vimont, A.; Daturi, M.; Hamon, L.; De Weireld, G.; Chang, J.-S.; Hong, D.-Y.; Kyu Hwang, Y.; Hwa Jhung, S.; Férey, G. High Uptakes of CO2 and CH4 in Mesoporous Metal—Organic Frameworks MIL-100 and MIL-101. *Langmuir* **2008**, *24* (14), 7245–7250. https://doi.org/10.1021/la800227x.

(30) Celeste, A.; Borondics, F.; Capitani, F. Hydrostaticity of Pressure-Transmitting Media for High Pressure Infrared Spectroscopy. *High Press. Res.* **2019**, *39* (4), 608–618. https://doi.org/10.1080/08957959.2019.1666844.

(31) Prescher, C.; Prakapenka, V. B. DIOPTAS: A Program for Reduction of Two-Dimensional X-Ray Diffraction Data and Data Exploration. *High Press. Res.* **2015**, *35* (3), 223–230. https://doi.org/10.1080/08957959.2015.1059835.

(32) Gonzalez-Platas, J.; Alvaro, M.; Nestola, F.; Angel, R. EosFit7-GUI: A New Graphical User Interface for Equation of State Calculations, Analyses and Teaching. *J. Appl. Crystallogr.* **2016**, *49* (4), 1377–1382. https://doi.org/10.1107/S1600576716008050.

(33) Birch, F. Finite Elastic Strain of Cubic Crystals. *Phys. Rev.* **1947**, *71* (11), 809–824. https://doi.org/10.1103/PhysRev.71.809.

(34) Chapman, K. W.; Halder, G. J.; Chupas, P. J. Pressure-Induced Amorphization and Porosity Modification in a Metal–Organic Framework. *J. Am. Chem. Soc.* **2009**, *131* (48), 17546–17547. https://doi.org/10.1021/ja908415z.

(35) Vimont, A.; Goupil, J.-M.; Lavalley, J.-C.; Daturi, M.; Surblé, S.; Serre, C.; Millange, F.; Férey, G.; Audebrand, N. Investigation of Acid Sites in a Zeotypic Giant Pores Chromium(III) Carboxylate. *J. Am. Chem. Soc.* **2006**, *128* (10), 3218–3227. https://doi.org/10.1021/ja056906s.

(36) Thibaud, J.-M.; Rouquette, J.; Hermet, P.; Dziubek, K.; Gorelli, F. A.; Santoro, M.; Garbarino, G.; Alabarse, F. G.; Cambon, O.; Di Renzo, F.; van der Lee, A.; Haines, J. High-Pressure Phase Transition, Pore Collapse, and Amorphization in the Siliceous 1D Zeolite, TON. *J. Phys. Chem. C* **2017**, *121* (8), 4283–4292. https://doi.org/10.1021/acs.jpcc.6b11594.

(37) Wu, H.; Yildirim, T.; Zhou, W. Exceptional Mechanical Stability of Highly Porous Zirconium Metal–Organic Framework UiO-66 and Its Important Implications. *J. Phys. Chem. Lett.* **2013**, *4* (6), 925–930. https://doi.org/10.1021/jz4002345.

(38) Sapnik, A. F.; Johnstone, D. N.; Collins, S. M.; Divitini, G.; Bumstead, A. M.; Ashling, C. W.; Chater, P. A.; Keeble, D. S.; Johnson, T.; Keen, D. A.; Bennett, T. D. Stepwise Collapse of a Giant Pore Metal–Organic Framework. *Dalton Trans.* **2021**, *50* (14), 5011–5022. https://doi.org/10.1039/D1DT00881A.

(39) Ying, P.; Zhang, J.; Zhong, Z. Pressure-Induced Phase Transition of Isoreticular MOFs: Mechanical Instability Due to Ligand Buckling. *Microporous Mesoporous Mater.* **2021**, *312*, 110765. https://doi.org/10.1016/j.micromeso.2020.110765.

(40) Robison, L.; Drout, R. J.; Redfern, L. R.; Son, F. A.; Wasson, M. C.; Goswami, S.; Chen, Z.; Olszewski, A.; Idrees, K. B.; Islamoglu, T.; Farha, O. K. Designing Porous Materials to Resist Compression: Mechanical Reinforcement of a Zr-MOF with Structural Linkers. *Chem. Mater.* **2020**, *32* (8), 3545–3552. https://doi.org/10.1021/acs.chemmater.0c00634.

(41) Chui, S. S.-Y.; Lo, S. M.-F.; Charmant, J. P. H.; Orpen, A. G.; Williams, I. D. A Chemically Functionalizable Nanoporous Material [Cu3(TMA)2(H2O)3]n. *Science* **1999**, *283* (5405), 1148–1150. https://doi.org/10.1126/science.283.5405.1148.

(42) Dan-Hardi, M.; Serre, C.; Frot, T.; Rozes, L.; Maurin, G.; Sanchez, C.; Férey, G. A New Photoactive Crystalline Highly Porous Titanium(IV) Dicarboxylate. *J. Am. Chem. Soc.* **2009**, *131* (31), 10857–10859. https://doi.org/10.1021/ja903726m.

Table of Contents artwork

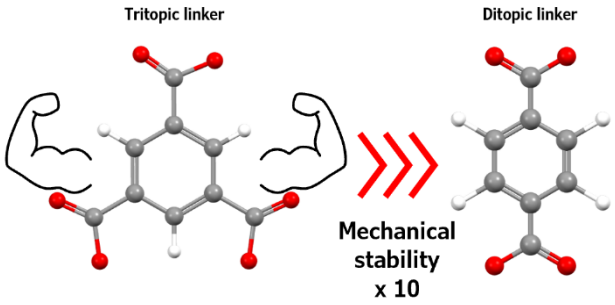
Tritopic linker
Ditopic linker
Mechanical
stability
x 10